NUMERICAL INVESTIGATION OF THE MOLD FILLING BEHAVIOR OF SANDWICH PARTS IN RESIN TRANSFER MOLDING

S. Dietrich[1], J. Seuffert[1] and L. Kärger[1]

[1] Institute of Vehicle Systems Technology (FAST), Karlsruhe Institute of Technology (KIT), Karlsruhe, Germany, email: sarah.dietrich@kit.edu, web: https://www.fast.kit.edu/lbt

Keywords: Fluid Structure Interaction, RTM process simulation, porous solid mechanics, Terzaghi's law, Finite Volume Method

ABSTRACT

In this work a simulation method for the mold filling in resin transfer molding is propsed and discussed at the application example of manufacturing a sandwich part with embedded foam core.

The resin flow is modelled as Darcy flow through a porous medium which is coupled over an internal fluid structure interaction to the deformation of the porous domain, as the fabric deforms due to external forces and the resin pressure. The fabric deformations are calculated using Terzaghi's law of effective stress. The porous domain consisting of fabric and resin is coupled to the solid domain, which models the foam core, via another fluid structure interaction.

The simulation results obtained with this approach are examined with regard to their sensitivity to input parameters such as the compression modulus of the foam core and fiber semi-finished product.

It is observed that the deformation of the foam core has a huge influence on the pressure in the fluid domain as a balance of forces between solid and fluid domain causes the pressure to asymptotically approximate a maximum value, depending on the compression behavior of the foam material, while it is linearly increasing with rigid core.

1 INTRODUCTION

Sandwich parts with fiber reinforced cover layers are of high interest as structural parts because of their high weight-specific bending stiffness. One way of manufacturing those parts in one process step is Resin Transfer Molding (RTM) with embedded foam cores [1]. However, modelling the infiltration process is challenging as many defects like core shift or deformation can occur [2] due to the fluid pressure and fabric compaction. As the foam core deforms, the fluid domain changes which affects fiber volume fraction, compaction behavior and fluid pressure. This interdependent influence can be accounted for by an internal and external Fluid-Structure-Interaction (FSI) approach.

The mold filling behavior in RTM with embedded foam cores was studied experimentally and with a one-dimensional analytical model by Binetruy and Advani [3]. They reported a good agreement between both methods but highlighted that more sophisticated models for the core material are necessary. A similar mold-filling behavior was observed by Deleglise et al. [4] in RTM and Compression RTM (CRTM) with a two-dimensional model for the fluid flow coupled to a one-dimensional spring model for the foam core. Both publications are omitting the deformation of the porous fiber-preform and limited to simple geometries or specific applications due to the assumption of one- or two-dimensional behavior.

In this work a three-dimensional finite volume approach is used to model the mold filling behavior, including interaction between the compressing fiber preform and the infiltrating resin by means of an internal FSI and a compressible two-phase flow to account for the escaping air. This approach is coupled to a three-dimensional finite element model of the foam core to model the FSI between resin flow and core material at the deformable interface.

2 SIMULATION APPROACH

2.1 Fluid Flow

To model the Fluid flow through a porous medium a porous drag term based on Darcy's Equation [5] is added as source term in the conservation of momentum equation:

$$\boldsymbol{Q}_{\mathrm{Darcy}} = \nabla p_{\mathrm{Darcy}} = -\mu \boldsymbol{K}^{-1}(1-\varphi)\boldsymbol{u}\,, \tag{1}$$

where μ denotes the dynamic fluid viscosity, $\boldsymbol{u}$ is the velocity, ∇p the pressure gradient, φ the fiber volume fraction (fvf) of the porous domain and $\boldsymbol{K}$ the permeability tensor of the fiber-preform. The permeability tensor is defined in the principal axis system and rotated in fiber-direction in each cell.

2.1 Finite Volume poro-elasticity and internal FSI

An existing mold-filling simulation approach for RTM with non-constant cavities [6,7] has been extended for compressible fiber materials and for FSI with a deformable core. The compaction behavior of the fiber semi-finished product is modelled with an internal FSI based on the finite volume approach for solid mechanics introduced by Cardiff [8] and extended by Tang et al. [9] for poro-elasticity using Terzaghi's law [10] for effective stress inside a porous medium:

$$\sigma_{\mathrm{total}} = \sigma_{\mathrm{eff}} - p\mathbf{I}, \tag{2}$$

where p is the fluid pressure inside the porous medium, adding an additional normal stress inside the solid. The poro-elasticity is described using an updated lagrangian approach. The advantage of this approach is that in each time increment the current deformations are set as reference configuration and thus the initial deformation defaults to zero in each increment. Thus, the updated Green-Lagrange strain increment can be expressed in terms of the incremental displacements $\delta\boldsymbol{d}$ as:

$$\delta\boldsymbol{E}_{\mathrm{u}} = \frac{1}{2}(\nabla\delta\boldsymbol{d} + \nabla\delta\boldsymbol{d}^{T} + \nabla\delta\boldsymbol{d}\cdot\nabla\delta\boldsymbol{d}^{T})\,, \tag{3}$$

where the index u marks the updated form.

Stress and strain are related with the St. Venant-Kirchhoff hyper-elastic constitutive equation:

$$\boldsymbol{S} = 2\mu_L\boldsymbol{E} + \lambda_{\mathrm{L}}\, tr(\boldsymbol{E})\,\boldsymbol{I} = \mathbb{C} : \boldsymbol{E}\,, \tag{4}$$

where μ_{L} and λ_{L} are the Lamé-constants of the porous fiber material, $\mathbb{C}$ is the stiffness tensor, and $\boldsymbol{S}$ is the 2nd Piola-Kirchhoff stress tensor.

The conservation equation of linear momentum can be written in terms of the 2nd Piola-Kirchhoff stress tensor and considering Terzaghi's law (Eqn (2)) as:

$$\frac{\partial}{\partial \mathrm{t}}\int_{\Omega}\rho\frac{\partial\boldsymbol{d}}{\partial \mathrm{t}}\mathrm{d}\Omega = \oint_{\Gamma}\boldsymbol{n}\cdot \mathrm{J}\mathbf{F}^{-\mathrm{T}}\cdot(\mathbf{S}_{\mathrm{eff}} - \mathrm{p}\mathbf{I})\cdot\mathbf{F}\,\mathrm{d}\Gamma + \int_{\Omega}\rho\boldsymbol{b}\,\mathrm{d}\Omega \tag{5}$$

Where b denotes body forces, F is the deformation gradient and $J = \det(F)$ the Jacobian.

The current area element $\mathrm{d}\boldsymbol{\Gamma}_{\mathrm{u}}$ can be derived from the initial area element $\mathrm{d}\boldsymbol{\Gamma}_0$ by Nanson's equation $\mathrm{d}\boldsymbol{\Gamma}_{\mathrm{u}} = \mathrm{J}\boldsymbol{F}^{-\mathrm{T}}\boldsymbol{\Gamma}_0$ [11]. Moreover, body forces can be neglected as the thickness direction is very small compared to the other dimensions, meaning that gravity forces are neglectable.

Thus, Variation of Equation (5) and transferring it into the updated configuration leads to:

$$\begin{aligned}\frac{\delta}{\delta t}\int_{\Omega}\rho_{\mathrm{u}}\frac{\delta(\delta\boldsymbol{d})}{\delta t}\,\mathrm{d}\Omega = &\oint_{\Gamma_{\mathrm{u}}}\boldsymbol{n}_{\mathrm{u}}\cdot\big(\delta\boldsymbol{S}_{\mathrm{eff,u}} - \delta p\boldsymbol{I}\big)\cdot\mathbf{F}_{\mathrm{u}}\,\mathrm{d}\Gamma_{\mathrm{u}}\\ &+\oint_{\Gamma_{\mathrm{u}}}\boldsymbol{n}_{\mathrm{u}}\cdot\big(\boldsymbol{S}_{\mathrm{eff,u}} - p\boldsymbol{I}\big)\cdot(\delta\mathbf{F})_{\mathrm{u}}\,\mathrm{d}\Gamma_{\mathrm{u}}\\ &+\oint_{\Gamma_{\mathrm{u}}}\boldsymbol{n}_{\mathrm{u}}\cdot\big(\delta\boldsymbol{S}_{\mathrm{eff,u}} - \delta p\boldsymbol{I}\big)\cdot(\delta\mathbf{F})_{\mathrm{u}}\,\mathrm{d}\Gamma_{\mathrm{u}}\,.\end{aligned} \tag{6}$$

It is used that the deformation gradient in the initial configuration equals the unity tensor as the initial displacement gradient vanishes in the updated form.

The resulting updated incremental form of linear momentum using the St. Venant-Kirchhoff hyper-elastic constitutive equation (4):

$$\frac{\delta}{\delta t}\int_{\Omega}\rho_{\mathrm{u}}\,\frac{\delta(\delta\boldsymbol{d})}{\delta t}\,\mathrm{d}\Omega = \oint_{\Gamma_{\mathrm{u}}}\boldsymbol{n}_{\mathrm{u}}\cdot(2\mu_{\mathrm{L}}\delta\boldsymbol{E}_{\mathrm{u}} + \lambda_{\mathrm{L}}\,tr(\delta\boldsymbol{E}_{\mathrm{u}})\boldsymbol{I})\,\mathrm{d}\Gamma_{\mathrm{u}} - \oint_{\Gamma_{\mathrm{u}}}\boldsymbol{n}_{\mathrm{u}}\cdot(\delta p\,\boldsymbol{I})\,\mathrm{d}\Gamma_{\mathrm{u}} + \oint_{\Gamma_{\mathrm{u}}}\boldsymbol{n}_{\mathrm{u}}\cdot\left(\left[\boldsymbol{S}_{\mathrm{eff,u}} - p\boldsymbol{I} + \delta\boldsymbol{S}_{\mathrm{eff,u}} - \delta p\boldsymbol{I}\right]\cdot\nabla\delta\boldsymbol{d}\right)\mathrm{d}\Gamma_{\mathrm{u}} \tag{7}$$

is solved with a staggered implicit-explicit algorithm as proposed by Cardiff [8].

Therefore, the incremental strain tensor is replaced by its formulation in terms of incremental displacements, eqn. (3), and Equation (6) is reformulated to separate implicit and explicit parts:

$$\frac{\delta}{\delta t}\int_{\Omega}\rho_{\mathrm{u}}\,\frac{\delta(\delta\boldsymbol{d})}{\delta t}\,\mathrm{d}\Omega = \oint_{\Gamma_{\mathrm{u}}}(2\mu_{\mathrm{L}} + \lambda_{\mathrm{L}})\boldsymbol{n}_{\mathrm{u}}\cdot\nabla\delta\boldsymbol{d}\,\mathrm{d}\Gamma_{\mathrm{u}} + \oint_{\Gamma_{\mathrm{u}}}\boldsymbol{n}_{\mathrm{u}}\cdot\mathbf{Q}_{\Gamma}\,\mathrm{d}\Gamma_{\mathrm{u}} \tag{8}$$

where $\boldsymbol{Q}_{\Gamma}$ is a surface source term, consisting of the nonlinear parts, that are solved explicitly. [12]

$$\boldsymbol{Q}_{\Gamma} = \mu_{\mathrm{L}}\cdot(\nabla\delta\boldsymbol{d})^{T} + \lambda_{\mathrm{L}}tr(\nabla\delta\boldsymbol{d}) - (\mu_{\mathrm{L}} + \lambda_{\mathrm{L}})\nabla\delta\boldsymbol{d} + \mu_{\mathrm{L}}\nabla\delta\boldsymbol{d}\cdot\nabla\delta\boldsymbol{d}^{\mathrm{T}} + \frac{1}{2}\lambda_{\mathrm{L}}\,tr(\nabla\delta\boldsymbol{d}\cdot\nabla\delta\boldsymbol{d}^{\mathrm{T}} + \delta p\,\boldsymbol{I} + (S_{\mathrm{eff,u}} + \delta S_{\mathrm{eff,u}})\cdot\nabla\delta\boldsymbol{d} \tag{9}$$

As the source term is highly non-linear, it is solved by iterating over the solution until convergence is achieved.

The Fiber Volume Fraction φ and fiber orientation **ω** are updated in every increment depending on the deformation gradient:

$$\varphi_{\mathrm{u}} = \delta\det(\boldsymbol{F})^{-\mathbf{1}}\,\varphi \tag{10}$$

$$\boldsymbol{\omega}_{\mathrm{u}} = \delta\boldsymbol{F}^{-1}\cdot\boldsymbol{\omega}\cdot\delta\boldsymbol{F}^{-\mathrm{T}} \tag{11}$$

2.2 External FSI

The interaction between foam core and porous domain is considered with a partitioned approach due to the clearly defined interface, which allows different discretization approaches in the fluid and solid domain. While the porous medium is modelled with the finite volume approach in OpenFOAM [13] described above, the deformation of the foam core is calculated with finite elements in CalculiX [14].The coupling between the two approaches is handled by the coupling library preCICE [15].

The coupling library is called after each increment by the two participants and handles the time stepping, mapping and exchange of data at the interface. From the solid domain it retrieves a displacement and from the fluid domain a Force at the interface consisting of fluid pressure and fiber semi-finished product compaction forces. As the problem is strongly coupled an iterative approach is selected. Thus, the simulations and the data exchange are repeated for each time increment until a common solution is found.

3 SENSITIVITY STUDY

As the material behavior is complex and the coupling between fluid and solid domain is strong, a sensitivity analysis on a two-dimensional demonstration case is performed. For this purpose, a plate is used, where the width dimension is considered to be very large so as not to influence the filling and compaction behavior. The plate is built up of two fibrous layers with a foam core in between, that are placed in a mold. From one side the resin is injected into the fiber semi-finished product as depicted in Figure 1., while at the opposing site the surrounding pressure is used as outlet condition. For the first half second, the mold is compacted for 2 mm to its final Hight. The resin is injected with constant velocity $u_{\mathrm{in}} = 0.01\frac{\mathrm{m}}{\mathrm{s}}$ at the inlet. The injection flow rate is kept constant for 15 seconds even after the plate is fully filled to see what pressure evolves in a steady state flow.

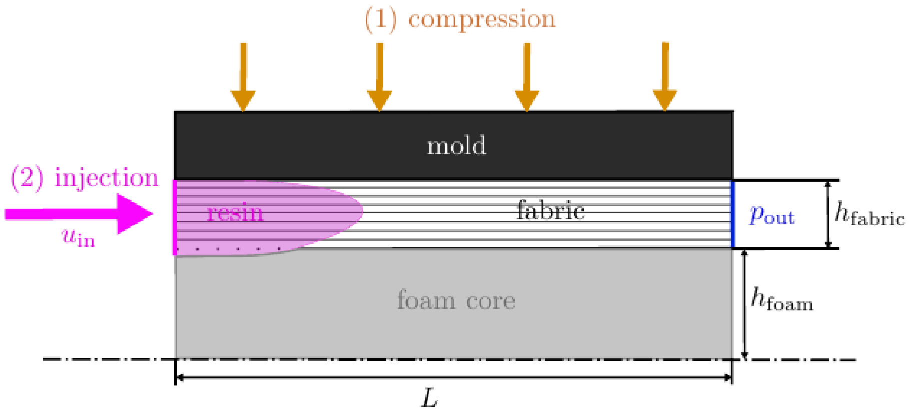

Fig. 1. Geometry, inlet (pink) and outlet (blue) position of the two-dimensional demonstration case. The dimension in in plane direction is assumed to be very large and thus neglectable. The case is assumed to be symmetric, thus only the upper half is considered, as depicted. The case consists of two steps: first the material is compressed by a constant displacement and second the resin is injected into the fibrous domain.

The resin viscosity is assumed to be constant with dynamic viscosity $\mu = 0.1$ Pa s. Curing as well as shear-rate or temperature dependent viscosity changes are neglected in a first approximation to limit the complexity of the model. The permeability is assumed to be isotropic and is defined dependent on the fvf. The foam core and fabric compaction behavior are modelled linear elastic. The Parameters used as basis for the sensitivity analysis are given in Table 1.

The Young's modulus of the foam core and fiber semi-finished product as well as the permeability and fiber volume fraction of the textile are varied to investigate the influence of these material parameters on the maximum pressure that evolves in the system due to a balance of forces between solid and fluid domain and on the maximum displacement at the interface.

For stability reasons the compaction is applied to the solid domain instead of the mold with a displacement-controlled boundary condition while the position of the mold is kept constant. Consequently, the initial displacement has a negative sign compared to the fluid pressure induced displacement.

Parameter	Value	Description
L	0.2 m	Flow length
$d_{c,0}$	0.002 m	Initial compression displacement
$h_{\mathrm{fabric},0}$	0.004 m	Initial fabric height
$h_{\mathrm{foam},0}$	0.02 m	Initial foam core height
E_{foam}	10 MPa	Young's modulus of the foam core
E_{fabric}	10 MPa	Young's modulus of the fabric at $\varphi = 0.5$
K_0	$10^{-10}\mathrm{m}^2$	Permeability at $\varphi = 0.5$
φ_0	0.25	Initial fvf (before compaction)

Table 1. Parameters used as standard values for the sensitivity analysis.

In Figure 2. And 3. the influence of the compaction behavior of foam core and fabric, respectively, on the maximum injection pressure and maximum height of the fluid domain are depicted. Both Young's moduli have a comparable influence on the interface displacement during the compaction phase. Additionally, the foam core Young's modulus influences the maximum injection pressure that evolves in the system during infiltration while the fabric compaction behavior has no huge influence on the pressure evolution.

The different foam core models are also compared to an approach with rigid core (violet), showing a significant reduction of pressure due to interface displacements depending on the foam core stiffness.

For the smallest foam core stiffness, the fluid domain is compacted to a final thickness of 2.65 mm instead of 2 mm and expands to 3.5 mm thickness during infiltration while the maximum pressure reaches 3.94 bar after 15 seconds of infiltration instead of 19 bar as with rigid core. For the rigid core the pressure rises linearly until the flow becomes a steady state while the pressure evolution is flattening for all simulations taking FSI into account.

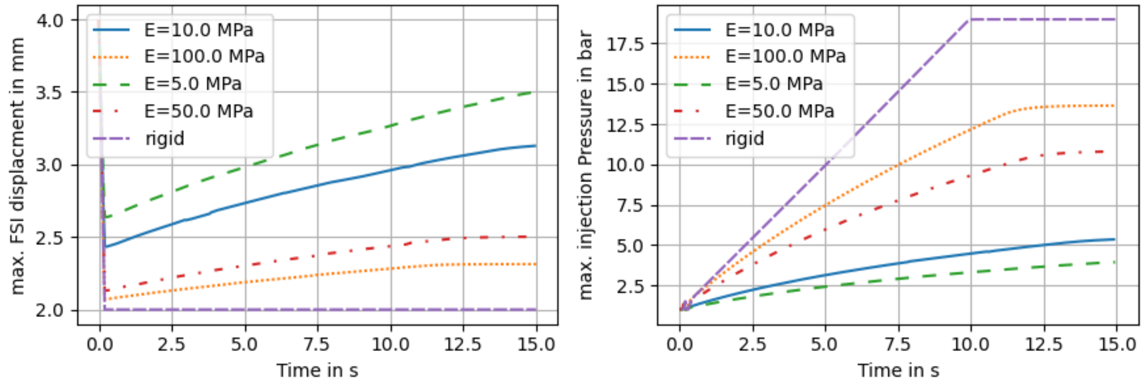

Figure 2. Maximum interface displacement (left) and maximum fluid pressure (right) over time for different foam core Young's moduli of 5 MPa (green), 10 MPa (blue), 50 MPa (red), 100 MPa (orange) and rigid foam core (violet).

In Figure 3. it becomes obvious that the Young's modulus of the fiber preform mainly influences the initial compaction during the compression step, where the height of the fluid domain varies between 2.25 mm and 3.2 mm for $E_{\text{fabric}} = 0.5$ MPa and $E_{\text{fabric}} = 10$ MPa, respectively. The displacements then approach to almost the same value of 3.25 mm height of the fluid domain during the injection phase. Only the hugest investigated Young's modulus of 10 MPa leads to a higher fluid domain of 3.4 mm. The evolving pressures vary between 5.8 bar and 3.1 bar.

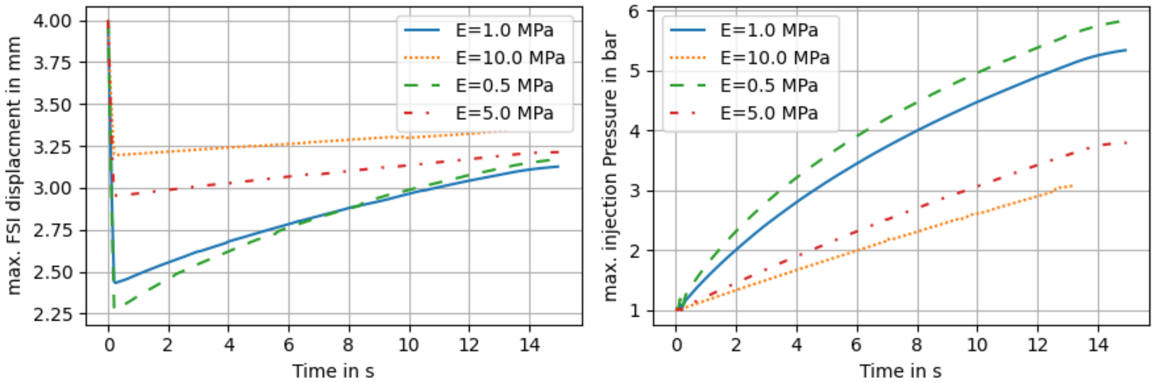

Figure 3. Maximum interface displacement (left) and maximum fluid pressure (right) over time for different fabric Young's moduli of 0.5 MPa (green), 1 MPa (blue), 5 MPa (red), and 10 MPa (orange).

In Figure 4. The target quantities are depicted over time for different permeabilities of the fiber semi-finished product. The fluid domain is compacted to a height of 2.43 mm for all permeabilities whereas it expands to more than 5 mm thickness during injection for the smallest permeability of 10^{-11}m^2 and stays almost constant for a permeability of 10^{-08}m^2. This behavior is almost proportional to the evolution of pressure. The results are similar for permeabilities of 10^{-08}m^2 and 10^{-09}m^2 because the Darcy Drag term becomes small in comparison to the viscous drag for this rather high permeabilities. The permeability doesn't influence the compression step but has a huge influence on pressure and displacement during the injection phase.

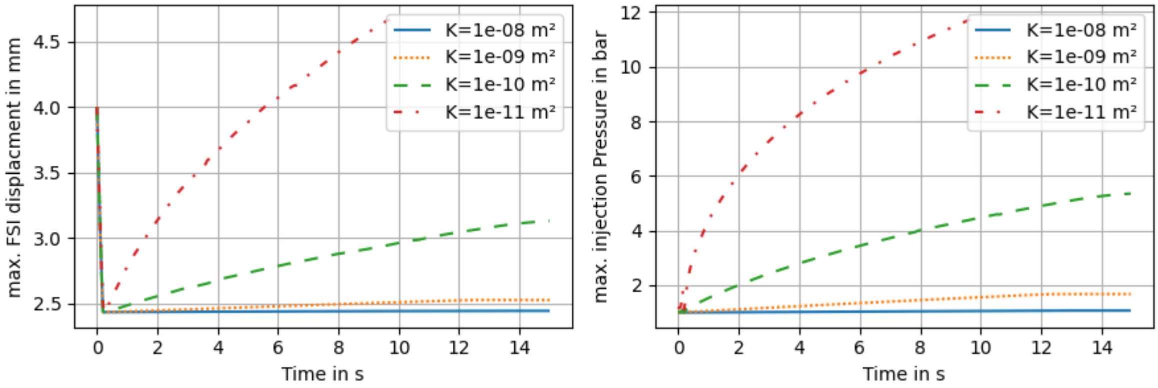

Figure 4. Maximum interface displacement (left) and maximum fluid pressure (right) over time for different fabric permeabilities of $10^{-08}\mathrm{m}^2$ (green), $10^{-09}\mathrm{m}^2$ (blue), $10^{-10}\mathrm{m}^2$ (red), and $10^{-11}\mathrm{m}^2$ (orange) at a FVF of 0.5.

The interface displacement and maximum fluid pressure for different initial FVFs are depicted in Figure 5. As the FVF has an impact on the compaction behavior as well as on the permeability of the fiber preform it influences the degree of initial displacement and the expansion of the fluid domain during the injection step.

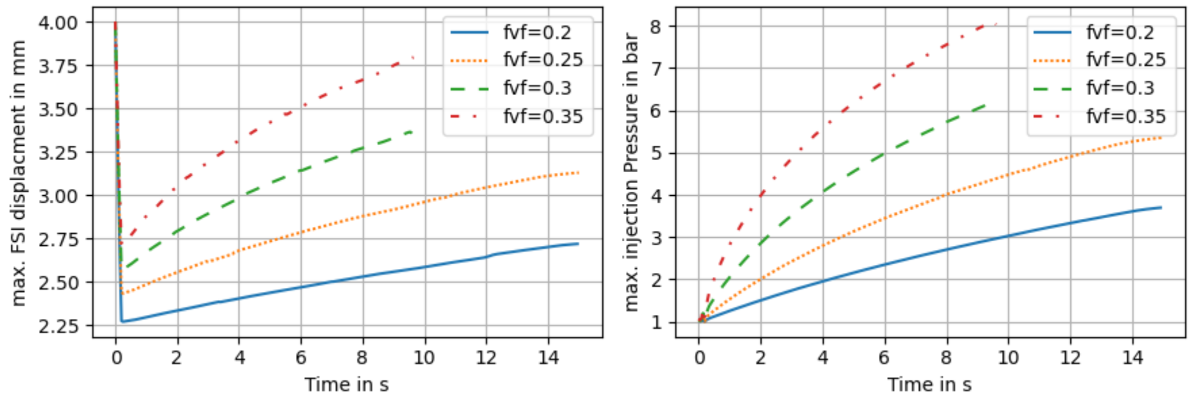

Figure 5. Maximum interface displacement (left) and maximum fluid pressure (right) over time for different fiber volume fractions of 0.2 (green), 0.25 (blue), 0.3 (red), and 0.35 (orange).

The infiltration time needed to fully impregnate the plate also varies for the different parameters investigated. But as the fluid domain is quite small, the time necessary to fill the domain is also small in comparison to the time investigated to examine the pressure evolution.

4 CONCLUSION

The deformations of the foam core have a huge influence on the filling behavior of the sandwich part and the necessary press forces and filling times. The pressure that evolves in the system is up to 4 times larger if a rigid core is assumed in comparison to an elastic foam core. Moreover, the displacement increases the volume that needs to be filled by the resin, increasing filling time and necessary amount of injected resin.

The proposed simulation approach is able to consider pressure changes and core deformations during the injection process. However, it is important to carefully characterize and model the material properties of foam, fiber semi-finished product and resin as they are strongly interacting and have a huge impact on the filling behavior.

Moreover, Temperature changes are not included in the model which might also affect the process as the foam core stiffness is strongly Temperature dependent and a huge effect of its stiffness on the filling pressure and interface displacements was identified in the numerical studies.

The filling behavior is influenced by the different material parameters of foam, resin and fiber preform. Thus, it is important to adequately model the reciprocal influence of fluid and solid domain.

ACKNOWLEDGEMENTS

The funding by the German Research Foundation (DFG) within the project "Modelling of the fluid-structure interaction in mold filling processes for an intrinsic manufacturing of fiber-reinforced composite sandwich components (FSI-Sandwich)" (project KA 4224/9-1 and HE 6154/8-1) is gratefully acknowledged.

REFERENCES

[1] Karlsson, K. F. and Aström, T., "Manufacturing and applications of structural sandwich components," *Composites Part A: Applied Science and Manufacturing, No.* 28, 1996, pp. 97–111.

[2] Al-Hamdan, A., Al-Ajloni, M., Alhusein, M., Rudd, C. D., and Long, A. C., "Behaviour of core materials during resin transfer moulding of sandwich structures," *Materials Science and Technology*, Vol. 16, 7-8, 2000, pp. 929–934.
doi: 10.1179/026708300101508711

[3] Binetruy, C. and Advani, S. G., "Foam Core Deformation During Liquid Molding of Sandwich Structures: Modeling and Experimental Analysis," *Journal of Sandwich Structures and Materials*, Vol. 5, No. 4, 2003, pp. 351–375.
doi: 10.1177/109963603027909

[4] Deleglise, M., Binetruy, C., and Krawczak, P., "Simulation of LCM processes involving induced or forced deformations," *Composites Part A: Applied Science and Manufacturing*, Vol. 37, No. 6, 2006, pp. 874–880.
doi: 10.1016/j.compositesa.2005.04.005

[5] Darcy, H., *Les Fontaines publiques de la ville de Dijon*, Dalmont, Paris, 1856.

[6] Seuffert, J., Rosenberg, P., Kärger, L., Henning, F., Kothmann, M. H., et al., "Experimental and numerical investigations of pressure-controlled resin transfer molding (PC-RTM)," *Advanced Manufacturing: Polymer & Composites Science*, Vol. 6, No. 3, 2020, pp. 154–163.
doi: 10.1080/20550340.2020.1805689

[7] Seuffert, J., Kärger, L., and Henning, F., "Simulating Mold Filling in Compression Resin Transfer Molding (CRTM) Using a Three-Dimensional Finite-Volume Formulation," *Journal of Composites Science*, Vol. 2, No. 2, 2018, p. 23.
doi: 10.3390/jcs2020023

[8] Cardiff, P., "Development of the Finite Volume Method for Hip Joint Stress Analysis," Dissertation, 2012.

[9] Tang, T., Hededal, O., and Cardiff, P., "On finite volume method implementation of poro-elasto-plasticity soil model," *International Journal for Numerical and Analytical Methods in Geomechanics*, Vol. 39, No. 13, 2015, pp. 1410–1430.
doi: 10.1002/nag.2361

[10] Terzaghi, K., *Erdbaumechanik auf bodenphysikalischer Grundlage*, Franz Deuticke, Leipzig, 1925.

[11] Bathe, K.-J., *Finite element procedures*, Prentice Hall, Englewood Cliffs, NJ, 1996, 1037.

[12] Seuffert, J., "Mold-filling Simulation of Resin Transfer Molding with Fluid-Structure Interaction," 2022.

[13] Weller, H. G., Tabor, G., Jasak, H., and Fureby, C., "A tensorial approach to computational continuum mechanics using object-oriented techniques," *Computer Methods in Applied*

Mechanics and Engineering, Vol. 12, No. 6, 1998, p. 620. doi: 10.1063/1.168744

[14] Dhondt, G., *The finite element method for three-dimensional thermomechanical applications,* Wiley, Chichester, 2005, 340.

[15] Chourdakis, G., Davis, K., Rodenberg, B., Schulte, M., Simonis, F., et al., "preCICE v2: A sustainable and user-friendly coupling library," *Open Research Europe*, Vol. 2, 2022, p. 51. doi: 10.12688/openreseurope.14445.2

[16] Poppe, C., Albrecht, F., Krauß, C., and Kärger, L., "A 3D Modelling Approach for Fluid Progression during Process Simulation of Wet Compression Moulding – Motivation & Approach," *Procedia Manufacturing*, 2020.

[17] Seuffert, J., *Resin Transfer Molding (RTM) of fiber-reinforced polymer sandwich parts: mold filling simulations with fluid structure interaction,* online, 2021.